ROTATIONAL-VIBRATIONAL RAMAN SPECTROSCOPY FOR MEASUREMENTS OF THERMOCHEMISTRY IN NON-ISOBARIC ENVIRONMENTS

A Thesis

by

ALEXANDER CHRISTIAN BAYEH

Submitted to the Office of Graduate Studies of
Texas A&M University
in partial fulfillment of the requirements for the degree of

MASTER OF SCIENCE

August 2009

Major Subject: Aerospace Engineering

ROTATIONAL-VIBRATIONAL RAMAN SPECTROSCOPY FOR MEASUREMENTS OF THERMOCHEMISTRY IN NON-ISOBARIC ENVIRONMENTS

A Thesis

by

ALEXANDER CHRISTIAN BAYEH

Submitted to the Office of Graduate Studies of
Texas A&M University
in partial fulfillment of the requirements for the degree of

MASTER OF SCIENCE

Approved by:

Chair of Committee,	Adonios Karpetis
Committee Members,	Rodney Bowersox
	Simon North
Head of Department,	Dimitris Lagoudas

August 2009

Major Subject: Aerospace Engineering

ABSTRACT

Rotational-Vibrational Raman Spectroscopy for
Measurements of Thermochemistry in Non-isobaric
Environments. (August 2009)
Alexander Christian Bayeh, B.S., Texas A&M University
Chair of Advisory Committee: Dr. Adonios N. Karpetis

The present work examines line measurements of pressure, temperature, and density in high speed, non-isobaric flows emanating from an underexpanded jet nozzle. Line images of rotational and vibrational Raman spectra are collected for a 8-mm linear laser probe, and are combined onto the same EMCCD detector. Combining the two techniques allows for a single-shot measurement of major species, pressure, and temperature in a turbulent non-isobaric environment that is chemically reacting. Temperature measurements along the laser test section are extracted from the rotational Raman spectrum, whereas major species densities are measured by examining the intensities of their respective vibrational Raman lines. Pressure can be calculated using an equation of state, in every location along the linear laser probe. The technique feasibility is examined by performing measurements of pressure, temperature and density in a non-reacting underexpanded air jet where the chemical composition is constant and known. Future work will extend the technique to chemically reacting supersonic flows with unknown chemical composition.

To William, Liela, Madeleine, and Samuel

ACKNOWLEDGMENTS

I would like to extend my gratitude to my advisor Dr. Adonios Karpetis, for guiding my research efforts, his continued support, and for pushing me to always do better. I would like to extend my gratitude to my committee members Dr. Rodney Bowersox and Dr. Simon North. Additionally, I would also like to thank Adam Johnson and Celine Kluzek for their support and assistance throughout this endeavor.

TABLE OF CONTENTS

Page

Page

LIST OF FIGURES

1. INTRODUCTION

1.1. General

Aerospace propulsion usually involves high-speed reacting flowfields where both turbulence and compressibility play important roles. Devices from turbine combustors to hypersonic scramjets very often utilize reacting flowfields under high Reynolds as well as Mach numbers. As the Ma number increases, local pressure variations in the flowfield become significant and the reacting flow cannot be considered isobaric (Linán and Williams, 1993). This physical picture is further complicated by the potential presence of several types of compression and rarefaction waves in compressible flows and their interaction with the turbulent field. The presented work describes the construction of a multiscalar measurement system for high-speed, non-isobaric, chemically reacting flows using line imaging of the combined rotational and vibrational Raman scattering. Temperature measurements along the laser test section are extracted from the rotational Raman spectrum, whereas major species densities are measured by examining the intensities of their respective vibrational Raman lines. Pressure can be calculated using an equation of state, in every location along the linear laser probe. The species densities can then be used to construct one the conserved scalars (i.e. the element mass fraction). The conserved scalar (or mixture fraction(Bilger et al., 1990)), ξ, characterizes the mixing state in non-premixed/partially premixed flames and stratified flows, while its dissipation rate can be defined as $\chi = 2D_{\xi}\nabla\xi\cdot\nabla\xi$ where D_{ξ} is a scalar diffusivity (Karpetis and Barlow, 2003) and can be thought of as the inverse of a characteristic time for mixing. The unique capability of the line-imaging multiscalar measurement techniques to quantify a local timescale everywhere

---

The journal model is *Combustion Science and Technology*.

in a turbulent flame cannot be over-stressed. As a derivative quantity, χ relies on the measurement -and squaring- of a gradient of ξ. The line-imaging technique can provide a 1-D 'surrogate' measure χ_{1D} of scalar dissipation if the conserved scalar ξ is measured along an axis (line) r with sufficient accuracy to form the differences$\Delta\ \xi$. By applying the line-imaging spectrometer to a chemically reacting, non-isobaric flow, one can examine the effects of both compressibility and turbulence on the chemistry of the reacting flow field.

1.2. Objective

The objective of this research is to design and construct a multiscalar line measurement Raman spectrometer capable of combining both vibrational and rotational spectra onto a single detector, and using a single laser. Once constructed, the next objective of the research is to perform an experiment with the spectrometer in the wake of an underexpanded air jet that is non-isobaric. The goal of the experiment is to be able to calculate the full thermochemistry (i.e. the density, temperature, and pressure) along an 8 mm section of the laser probe.

1.3. Previous Work

Past multiscalar measurement experiments concentrated in isobaric environments, under both atmospheric conditions (Nandula et al., 1994; Chen and Mansour, 1997; Karpetis and Barlow, 2003) as well as at elevated (constant) pressures (Tejeda et al., 1996; Cheng et al., 2002; Kojima and Nguyen, 2004). The measurement of local pressure using laser diagnostics is rather challenging, yet various techniques have been explored in the past. Two notable examples are Filtered Rayleigh Scattering (FRS) (Forkey et al., 1998; Miles et al., 2001) which combines planar thermometry

and velocimetry with pressure measurement yet cannot provide a local measurement of chemical composition, while Coherent Anti-Stokes Raman Spectroscopy (CARS) (Eckbreth, 1988; Foglesong et al., 1998) can provide only measurements of pressure and temperature in a single-point fashion.

2. EXPERIMENTAL SETUP

The experimental spectroscopy system consists of 3 subsystems: the laser and the optics for delivering pulses to the test section; the data acquisition system responsible for measuring the laser intensity in a single shot fashion; and the receiving optics/Raman spectrometer combination. The timing of the laser intensity measurements system and the EMCCD of the Raman spectrometer are dependent upon Q-switch and flash lamps of the laser, respectively. Preliminary experiments conducted with the spectroscopy system were conducted in the non-isobaric flow field in the wake of an underexpanded jet nozzle with an approximate exit Mach number of 2 and back pressure of about 60 psig.

2.1. Laser and Pulse Conditioning System

2.1.1. Laser

The second harmonic of a Nd:YAG laser at 532 nm was used for the laser system. The wavelength of each pulse was 532 nm and the pulse duration was initially 10 ns for Full Width at Half Max (FWHM). As seen in Equation (2.1), the higher the intensity of the pulse used to excite the molecules (I_0), the better the spectral signal that can be collected (I). The laser used in this study was capable of delivering a maximum pulse energy of approximately 1 Joule. This amount of energy per pulse when focused, however, leads to problems of dielectric breakdown of the air. This is due to large amounts of energy per unit area of air, and the dielectric breakdown process produces a spark that could potentially harm the spectrometer detector because of the broadband scattering involved in the process. Dielectric breakdown can be prevented using both an interferometric pulse stretcher and a Galilean telescope

as described in the next subsections.

$$I = \varepsilon I_o \Omega l N (\frac{\partial \sigma}{\partial \Omega}) \tag{2.1}$$

In this equation, I is the intensity of the Raman spectra collected; ε is an efficiency factor associated with the system; I_0 is the intensity of the light used to excite the molecules (the laser); Ω is the solid angle formed by the lens collecting light from the test section out of 4π steradians; l is the length of the probe volume that is being interrogated; N is the number density of the molecules in the probe volume; and $(\partial\sigma/\partial\Omega)$ is the Raman differential scattering cross-section (cm^2/steradian) (Eckbreth, 1988). This equation is phenomenologically based, but applies to all incoherent light scattering processes; namely Rayleigh and both vibrational and rotational Raman. For a coherent scattering process, such as CARS, the factor Ω is considered to be 4π because all of the scattered light is able to be collected.

2.1.2. Interferometric Pulse Stretcher

A single-leg pulse stretcher was constructed with a total length of 10 feet. The first element of the pulse stretcher is a 50/50 beam splitter. For each pass of the pulse stretcher, the pulse is retarded by 50% and sent into two directions: either towards the test section, or for another pass through the pulse stretcher where it is delayed by approximately 10 ns. This system results in a FWHM pulse of 25 μs, as compared to 10 ns of the original pulse.

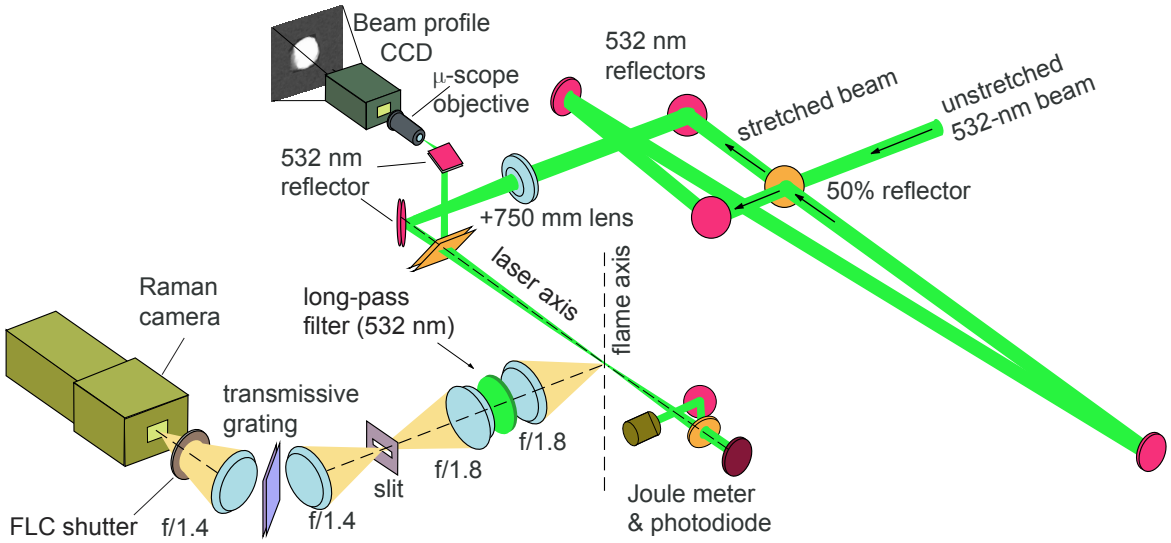

Figure 1. Schematic drawing showing the line imaging ro-vib Raman spectroscopy experiment: laser delivery (pulse stretcher, focusing lens and beam monitoring) and the Raman imaging system (transmissive-grating spectrometer).

2.1.3. Telescope

Another common cause of dielectric breakdown in air is non-uniformity in the laser beam cross-section. Instead of having a cross-section with an even distribution of energy, a problem that can occur is having nonuniform areas of high and low power flux. When focused by the laser delivery system, these areas of high power flux also lead to dielectric breakdown. Another potential problem of having these high energy density areas in the beam cross-section is that they could potentially 'burn' in the beam path. One way to avoid inhomogeneities in the beam is to simply propagate the laser pulse through a lens (Zhou et al., 2007). In order to smooth the profile out and to prevent damaging the optics of the pulse stretcher, a reversed Galilean telescope was placed just prior to the pulse stretcher, also seen in Fig. 1. The telescope is

constructed out of two lenses: a 300 mm negative lens, followed by a 500 mm positive lens. These two lenses, in the reversed order of a traditional Galilean telescope, expanded the beam rather than condensing it. This therefore distributed the laser energy over a larger area, and in effect reduced the energy density encountered by each element of the pulse stretcher. By doing so, this also reduced the risk of damaging the mirrors used in the pulse stretcher.

The relative positioning lenses and overall expansion of the beam through the telescope can be calculated using simple relations. The separation of the lenses is found by simply adding the focal lengths of the two difference lenses (Eckbreth, 1988). Since the 300 mm lens is negative, however, it would be subtracted from the value of the 500 mm lens. This gives us a separation distance of 200 for the telescope lenses. The beam first encounters the 300 mm negative lens. This begins the expansion process by de-collimating the pulse of the laser, and sending it on a diverging path. The pulse then encounters the 500 mm lens where it is re-collimated.

Ray tracing can be performed to calculate the magnification that each pulse undergoes. This is done using a combination of ray tracing matrix operations for thin lenses and a homogeneous medium (Fowles, 1989). These matrix equations can be compounded to represent the transformation that a pulse would undergo as it passes through the reversed telescope. Equation (2.2) shows the respective expansion that a laser pulse would undergo. In this equation r_1 and r_2 represent the radii of the beam prior to the telescope and after exiting the telescope, respectively.

$$\frac{r_2}{r_1} = -\frac{f_2}{f_1} \tag{2.2}$$

It should be noted that each pulse that enters the reversed telescope is collimated, and therefore as a result also exits the telescope collimated. Therefor the initial beam diameter of 9 mm prior to entering the reversed telescope, is expanded to a diameter of 15 mm.

2.1.4. Focusing Lens

Once a laser pulse passes through the reversed telescope and the interferometric pulse stretcher, it is then sent to the focusing lens prior to entering the test section. By examining the scattered photons at the focal point where the beam is the smallest, it is possible to resolve smaller features within the probe volume when scanning it. One feature of the system that helps to provide a smaller focal point is the reversed telescope. The airy disk which contains 84% of the energy transmitted by the focusing lens (Eckbreth, 1988), at the focal point has a diameter d given by Equation (2.3), and is a function of both wavelength λ and the diameter of the laser beam prior to encountering the focusing lens D ($2r_2$).

$$d = 2.44\frac{f\lambda}{D} \tag{2.3}$$

Using the parameters of the optical system we can calculate a beam waist diameter of 65 μm. The diameter is inversely proportional to the inlet diameter D of the laser, and therefore by expanding the beam at the telescope prior to the focussing lens it is possible to focus the beam down to a smaller radius. However, since the lens is not diffraction limited, and the beam profile is closer to a 'top hat' uniform profile, rather than a Gaussian profile, the waist diamter will not be as small as predicted by the equation above. Using burn paper placed at the focal point of the laser, it was

determined that the diameter of the laser core at the focal point was approximately 250 μm.

2.2. Laser Intensity Measurement System

The laser energy can vary slightly with every pulse that is generated. As seen in Equation (2.1), the signal that is collected is directly proportional to the laser intensity. Therefore because the intensity of the laser varies from pulse to pulse it is important to implement a system that measures the intensity of every pulse and records it for the purpose of performing normalization calculations (Laurendeau, 1988). This system consists of a photodiode that measures the intensity of each laser pulse, a boxcar sample-and-hold integrator and amplifier that stores the measured value of the photodiode, and the data acquisition system that retrieves and stores the data from the boxcar.

In order to measure laser intensity, a small fraction of each laser pulse is diverted to a photodiode with neutral density filters in place to prevent saturation (or even possible damage) of the diode itself. The output signal from the diode is then stored externally using a boxcar averager. The acquisition time gate of the boxcar is set to be wide enough to capture the entire pulse width in time (approximately 30 ns), and the signal of the photodiode over this gated time interval is then integrated by the boxcar. In order to initiate the acquisition process, the boxcar is triggered using the TTL output signal of the laser Q-switch, and the delay of the acquisition gate in then adjusted such that the signal from the photodiode falls within the gate. The alignment of the gate and photodiode signal in time is performed using an oscilloscope to examine their relative positions in real-time. Once the signal of the photodiode is integrated, its value is sampled held on the boxcar for computer interrogation, until

the the next laser pulse is initiated, and the process is repeated for every shot. The computer designated to collect the data from the boxcar is triggered to interrogate it only when the camera for collecting the spectra captures an image. This ensures that for every spectral image collected there exists a measurement of corresponding laser energy for normalization purposes.

2.3. Raman Spectrometer

The Raman spectrometer consists of various optical elements that are responsible for collecting, filtering, and dispersing the scattered light from the test section to the Electron Multiplying Charge Coupled Device (EMCCD) detector. Because the system is capable of performing line imaging measurements, the detector will form a 2-D image consisting of both a spatial axis and a wavelength axis. As will be discussed subsequently, the system has a 1:1 conjugation from the width of the pixels on the detector to the axis of the laser. This forms the spatial axis of the image captured. Each column of pixels forms the spectra of the gases contained within the probe volume of the laser corresponding to that location in space. Because each column of pixels forms the spectra of of the gases within it's respective probe volume, the second axis of each image formed by the detector corresponds to wavelength. This is due to dispersion of the collected light by a diffraction grating contained within the optical components of the spectrometer.

The first element of the Raman spectrometer that is encountered is an 85 mm $f/1.8$ Nikkor lens that is responsible for collecting scattered light from the test section. This lens collects light from a solid angleΩ , which appears in Eqn. (2.1), and can be calculated as follows:

$$\Omega = \int_0^{2\pi} \int_0^{\theta_h} sin\theta d\theta d\phi \tag{2.4}$$

$$\theta_h = tan^{-1} \frac{d}{2f} \tag{2.5}$$

where θ_h is the planar half angle subtended by the lens and can be calculated, d is the diameter of the lens (47.2 mm), and f is the focal length of the lens (85 mm). For the described 85 mm $f/1.8$ length, the half angle θ_h is calculated to be .271 radians, and thus yields a value for Ω of .229 steradians.

Once the scattered light has been collected by the lens, it is then collimated and refocused using an identical 85 mm $f/1.8$ lens in a reversed configuration to minimize aberrations. An ultra-sharp long-pass filter is inserted within the collimated region between the matched lenses. This filter is a key component to the experiment, and allows for the capability to collect both vibrational and rotational spectra on the same detector. The differential scattering cross section for Rayleigh scattering is approximately three orders of magnitude larger than that of Raman scattering, and hence if the Rayleigh signal were imaged on the detector along with both the rotational and vibrational spectra, the detector would be saturated by the Rayleigh signal alone, and measurements of the different Raman spectra would not be possible. The initial cut-off wavelength of the filter is approximately 536 nm, but can be adjusted to be closer to the laser wavelength (532 nm). Figure (2) shows the response of the filter provided by the manufacturer (Semrock) prior to angle tuning. The feature that should be noted in Figure 2 is the sharp response at its design wavelength.

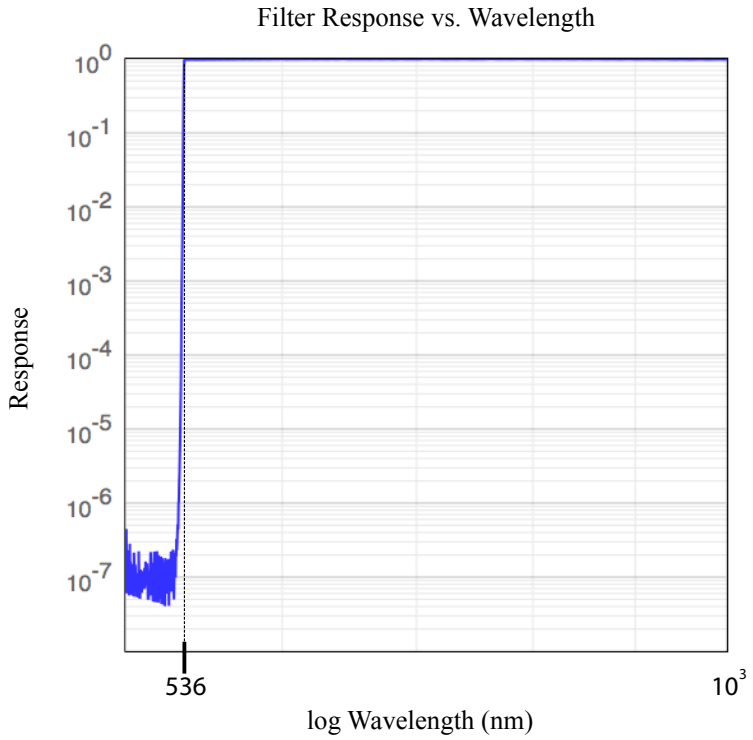

Figure 2. Long pass filter response vs. wavelength

It is important to adjust the light cutoff wavelength as close to 532 nm as possible in order to capture as much of the pure rotational spectra as possible, and thus increase the accuracy of the temperature measurement. The filter can be angle tuned to adjust the cutoff wavelength of the filter. To adjust the cut-off wavelength of the filter to approximately 534 nm, the angle of incidence of the filter (θ), was adjusted to about 10°. The equation for process was provided by the manufacture (Semrock), and is shown as follows:

$$\lambda = \lambda_0(1 - (\frac{sin\theta}{\eta_{eff}})^2)^{1/2} \tag{2.6}$$

For the angle tuning equation the parameter λ represents the transformed wavelength, λ_0 is the original wavelength, θ is the incidence angle of the filter with respect to the path of the light, and η_{eff} is the effective index of refraction of the filter. This transformation is applied to the wavelength of each point for the filter response to calculate the new corresponding wavelengths. When the cut-off wavelength is moved closer to the wavelength of the laser, a larger portion of the rotational Raman spectrum is allowed to pass through for temperature calculation, while still filtering out the intense Rayleigh signal.

Once the light is focused through the second $f/1.8$ lens, it passes through a 250 μm slit that defines the laser probe volume. The slit also provides the advantage of blocking out any excess background light that may be entering the spectrometer through the collection lens. This excess light is prevented from reaching the detector, and as a result the background noise contribution is less. The light is then re-collimated between a set of 50 mm $f/1.4$ Nikon Nikor lenses. Once the light is collimated by the first lens, it passes through a transmissive diffraction grating that introduces wavelength dispersion. Equation (2.7) is used to calculate the incidence angle of the holographic diffraction grating:

$$d(sin\theta_m + sin\theta_i) = m\lambda \tag{2.7}$$

For this relationship d is the grove spacing of the grating, θ_i is the angle of incidence of the grating with the incoming collimated light, and θ_m is the angle for which the light at wavelength λ and diffraction order m is oriented relative to the surface normal of the grating once the light has passed through it (Eckbreth, 1988). To calculate the angle at which the diffraction grating should be relative to the incoming collimated

light, θ_m is set equal to θ_i and the parameters of the grating are entered into the equation. For the grating being used, d is 833 nm, and 600 nm is the central wavelength. Here, m is set to 1 because the fisrt diffraction order is typically the strongest. The value calculated for θ_i was 21.1°. This value was also used for θ_m when placing the second 50mm $f/1.4$ relative to the diffraction grating. In order to do this, the lens and camera were mounted on an elevated platform that was angled approximately 21.1° relative to the diffraction grating as seen in Figure 3.

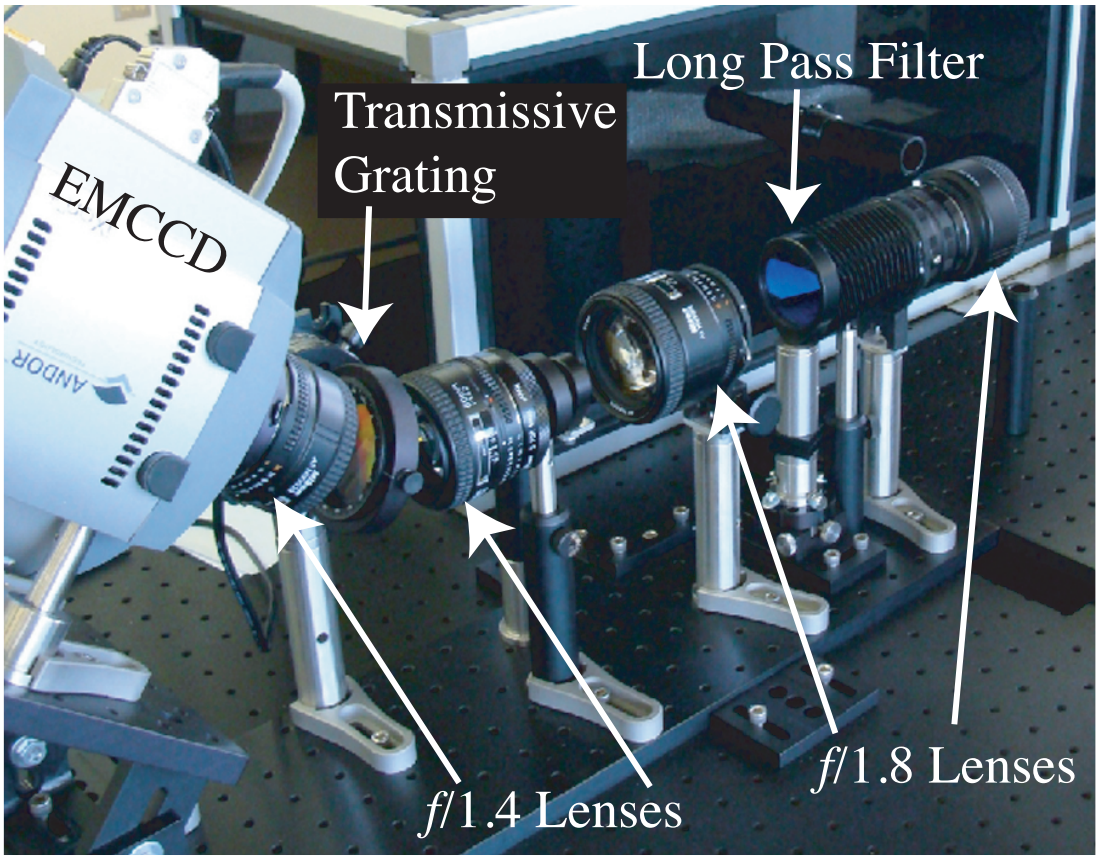

Figure 3. Image of the Raman spectrometer as constructed in the lab

The final element of the Raman spectrometer is the EMCCD detector which images the spectra along a portion of the laser. The 2-D image formed on the detector gives wavelength on the verticle axis due to the dispersion introduced by the transmissive grating, and space on the horizontal axis that correlates to physical space along the laser axis because of the 1:1 conjugation of the spectrometer's optical system. The EMCCD detector (Andor iXon 897) is a back-illuminated CCD device with 512×512 pixels of 16 μm resolution and high Quantum Efficiency ($\approx 90\%$). The detector provides four aspects that are of critical importance to the measurement of low-level signals: hardware pixel binning, thermo-electric cooling, frame transfer capability, and electron multiplication of the signal. Hardware pixel binning allows for the possibility of combining multiple pixels on the detector into 'superpixels' and interrogating their combined collected charge through the Analog-to-Digital (A/D) converter in one clock period. The Signal-to-Noise Ratio (SNR) of hardware binning is higher than one provided by software binning; however, both techniques offer higher SNR than single-pixel acquisition. Thermo-electric cooling to low temperatures (approximately -100°C) virtually eliminates the thermal electron noise (Dark current) from the detector, while the presence of two CCDs within the detector head allows for fast frame transfer operation that suppresses the background noise. The detector chip itself contains two CCD arrays that are adjacent to each other. This functionality allows for the possibility of image capturing without the need of an external shutter and thus reduces the complexity of the experimental setup, at least when compared to past multiscalar Raman measurement systems that relied on fast mechanical shutters (Miles and Barlow, 2000). A Ferroelectric Liquid Crystal (FLC) shutter has also been used in early phases of this work, as shown in Figure 1, yet the measurements that will be presented subsequently were conducted without using a shutter. The final aspect of the EMCCD device is the solid state electron-multiplication register

row built in prior to the A/D converter. This additional amplification stage relies on numerous (e.g. 512) multiplication registers, each of which amplifies the analog signal by a very small amount (e.g. 1%) through a process of impact ionization. The EMCCD technology allows for the fast detection of low-light signals by suppressing the read-out noise associated with the A/D conversion and transfer at fast data rates (Mackay et al., 2001). Pretriggering of the EMCCD detector and synchronization with the laser timing, as well as the the laser energy measurement system, were accomplished by using the TTL signal generated by the laser flash lamps and conditioning it through a variable delay pulse generator.

Photon-arrival statistics can be described by an underlying Poisson distribution, and as a result the standard deviation (noise) of the signal N is related to the actual signal (photon 'counts') P by the simple formula $N \sim P^{1/2}$. The SNR for a shot-limited (Poisson) process then becomes $SNR \sim P^{-1/2}$, signifying that large increases in signal levels lead to modest increase in SNR values. In actual imaging applications involving incoherent light scattering from a target a more involved formula may be used for the evaluation of SNR:

$$SNR = \frac{\dot{P}Q\tau}{[(\dot{P} + \dot{B})Q\tau + \dot{D}\tau + N_{A/D}^2]^{1/2}} \tag{2.8}$$

where τ is the exposure time of the imaging, $\dot{P}$ the signal photon arrival rate in s^{-1}, $\dot{B}$ the background photon arrival rate in s^{-1}, Q is the quantum efficiency of the detector, $\dot{D}$ the dark electron generation rate in s^{-1}, and $N_{A/D}$ is the read-out noise due to the Analog-to-Digital (A/D) conversion. This formula describes the SNR of a continuous-wave illumination, and therefore is more appropriate for a photographic imaging application. In the case of the experiment being performed using a pulsed laser source, the above formula must be modified to take into account the virtually

instantaneous, approximately within 25 ns, arrival of signal photons:

$$SNR = \frac{PQ}{[PQ + \dot{B}Q\tau + \dot{D}\tau + N_{A/D}^2]^{1/2}} \tag{2.9}$$

where P is the actual number of signal photons received onto the detector, and every other term is identical to the previous formula (Eckbreth, 1988). The EMCCD detector being used however, allows for simultaneous light acquisition in groups of pixels that are electronically equivalent to one large superpixel. If the group of M individual pixels forms a superpixel by hardware-binning onto the detector, the formula for SNR must be modified to:

$$SNR = \frac{MGPQ}{[MGPQ + M\dot{B}Q\tau + MG\dot{D}\tau + N_{A/D}^2]^{1/2}} \tag{2.10}$$

where G signifies the gain of the Electron-Multiplying capability of the EMCCD. It is worth noting that the terms for pixel-binning (M) and EMCCD gain (G) act in precisely the same fashion, but the former is an integer number, while the latter is a small real number that corresponds to the overall gain (values from 1 to 2).

2.4. Underexpanded Jet

In order to provide an experimental environment that offers varying pressure as well as optical accessibility for the laser and the collection optics, an underexpanded air jet was chosen as a target for the experiments. To produce an underexpanded jet for testing, a de Laval nozzle constructed from brass stock is attached to a tank of compressed air. As a fluid streamline passes the throat of the de Laval nozzle, it begins to expand and accelerate, causing the pressure along the axis of the nozzle to decrease. The nozzle is underexpanded if the pressure at its exit is greater than that

of the surrounding atmosphere, and contrary to that a nozzle is overexpanded if its exit pressure is less than that of the surrounding atmosphere. Once the flow from an underexpanded jet leaves the nozzle, the pressure of the flow has to come into equilibrium with the surrounding atmosphere. In order to do so the flow expands to the atmospheric pressure through an expansion fan. The expansion waves from the tip of the nozzle, for axisymmetric flow, pass through the centerline of the jet and interact with expansion fans emanating from all over the nozzle tip, as seen in Fig.4. After this, the expansion fans continue until they interact with the free jet boundary, i.e. a constant pressure slip line that encompasses the flow of the jet exhaust, and separates is from the surrounding stagnant atmosphere[1]. Once the expansion fans reach the constant pressure slip line, they are reflected off as compression waves. These compression waves then coalesce onto each other and form oblique shock waves that impinge on each other at the jet centerline, and then continue on to the free jet boundary as well. At this point the shocks are then reflected off as a new set of expansion fans, and the process begins once more. Each iteration of the process is successively weaker than the previous iteration due to entropy generation of the shocks, as well as viscosity. Finally after some amount of iterations, the jet flow is everywhere subsonic (John and Keith, 2006), and classic descriptions of viscous isobaric turbulent jets apply. A different variation of this occurs when the exit pressure at the tip of the nozzle is much greater than that of the atmospheric pressure. The flow is accelerated much more in this case because of the amount of expansion needed to attain equilibrium with the atmosphere. This increase in flow velocity prohibits the oblique shocks from interacting at the centerline; and thus to correct this, a normal shock is formed in the flow along with the associated shock triple point. A Mach disk

[1]The present discussion follows an inviscid approach. In real supersonic jet, viscosity introduces boundary layers in the place of the artificial velocity slip lines.

is formed when this shock is rotated about the axis of symmetry for the jet exhaust. Example schematics of both variations can be seen in Fig.4 with the slightly under-expanded jet on the left, and massively underexpanded jet on the right.

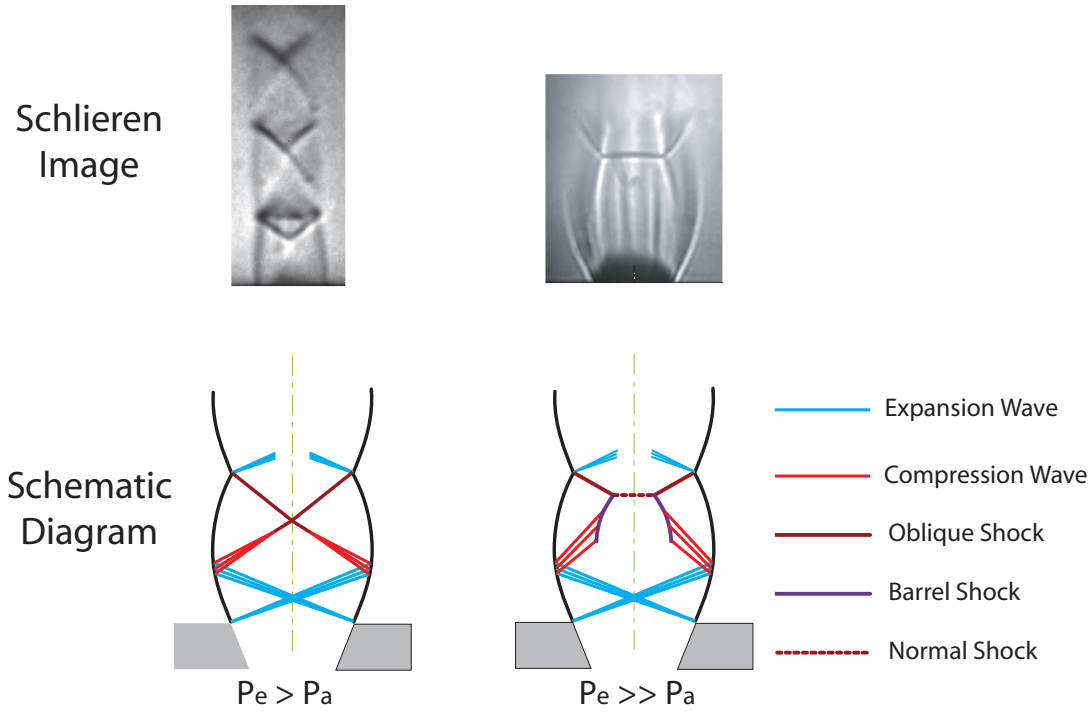

Figure 4. Schlieren images and schematic drawings of underexpanded jets

3. RESULTS AND SUMMARY

3.1. Measurements of Vibrational Spectra

The vibrational Raman spectra collected the laser beam provide a means for measuring densities of the species present within the probe volume. The technique relies on the measurement of the integrated intensities of the Q-branch Stokes vibrational intensities of all major species present. For the experimental results being presented for an underexpanded air jet, the only species that will be detected are N_2 (607 nm) and O_2 (580 nm), and as seen in Eqn. (2.1), the intensities for the spectra of each species present within the probe will be directly proportional to its number density within the probe volume. From this the densities of each species can be calculated, as well as their molar and mass fractions within each probe volume along the laser that is defined by the width of the superpixels constructed on the detector (Eckbreth, 1988). For future experiments involving flames, the major species that will be detected within the probe volume by the spectrometer additionally include CO_2, CO, CH_4, H_2O, and H_2. However, for these future experiments, broadband interference due to chemiluminescence and laser-induced fluorescence of minor species will be issues, and can be compensated for by the measurement of spectral content (signal) along a few positions where no Raman mode is active. A matrix inversion can then be implemented to account for cross-talk between spectral channels: each matrix element describes the cross-talk contribution (Masri et al., 1996; Hassel and Linow, 2000; Nguen et al., 1996; Kojima and Nguyen, 2004) and obtained by calibration against laminar flames of similar composition (Masri et al., 1996).

Since the present work introduces non-isobaric air flows with known composition, density calculations can performed utilizing only the N_2 vibrational spectra. The in-

tensity of the N_2 vibrational spectra is directly proportional to the number of N_2 molecules present within each probe volume superpixel, and therefore a similar number density for O_2 can be calculated using the already known ratio of molar fractions for air ($X_{N2} = .79$ and $X_{O2} = .21$). From here density can be calculated through the following relation:

$$\rho = AI_{N2}(MW_{N2} + \frac{X_{O2}}{X_{N2}} MW_{O2}) \tag{3.1}$$

The constant of proportionality A can be calculated if the density conditions of a probe volume are known. This value of A is then used in conjunction with the N_2 vibrational spectra to calculate the density along the laser probe.

3.2. Rotational Spectra

The techniques that utilize purely vibrational Raman scattering can,under suitable data processing, provide measurements of molar fractions X_i and density ρ, yet temperature can be calculated only in known isobaric environments using an ideal gas equation of state (Cheng et al., 2002). One of the contributions of the present research is the simultaneous application of a rotational Raman line imaging technique that allows for an independent measurement of rotational temperature, and hence pressure, in every superpixel along the laser probe. Spontaneous rotational Raman spectroscopy has been used many times in the past for the measurement of temperature, using both continuous wave (Fernández et al., 2006) and pulsed lasers (Kojima and Nguyen, 2004). The former approach is suitable only for long-time averaging in laminar flames, while the latter will be pursued here due to its capability for single-shot measurements in turbulent flames.

The rotational spectra for most species lie near the Rayleigh laser line at 532 nm, and this dictates the use of a very sharp long-pass filter in the spectrometer, such as the one used in the described system. From the vibrational Raman spectra the mole fractions X_i are used to form the expected theoretical rotational Raman spectrum, while in the present case X_i are known beforehand: the expected theoretical rotational Raman intensity is proportional to rotational populations, which are described by a Boltzmann distribution $N(J,T)$ (Schrader, 1995) at equilibrium:

$$N(J,T) = \frac{N_{tot}}{Q_{rot}} g_I (2J+1) e^{-BJ(J+1)hc/kT} \tag{3.2}$$

$$Q_{rot} = \frac{kT}{hcB} \tag{3.3}$$

$$B = \frac{h}{8\pi^2 cI} \tag{3.4}$$

Here N_{tot} is the total number density of the given species; Q_{rot}, given by Eqn.(3.3) is the rotational partition function; g_I is the nuclear spin degeneracy; J is the rotational level; B is the rotational constant, given by Eqn.(3.4); h is the Planck constant; c is the speed of light; k is the Boltzmann constant; T is the temperature of the species; and I is the molecular moment of inertia (Eckbreth, 1988). To convert the rotational levels J to wavelength for the S-Branch, and therefore convert the Boltzmann distribution to a function of wavelength rather than rotational level, the following relation is used.

$$\nu = \nu_0 - 4B(J + \frac{3}{2}) \tag{3.5}$$

The incident laser light frequency is given as ν_0, and ν is the associated frequency of the S branch transition for rotational level J. The associated wavelength can be

obtained from this by taking the inverse of ν. The calculations of the Boltzmann distributions for all species i, and varying temperature T can be used to "synthesize" the expected rotational spectra as:

$$RS(\lambda) = LP(\lambda) \sum_i X_i N_i(\lambda, T) \tag{3.6}$$

where I is the intensity of the synthesized spectra, $LP(\lambda)$ is the long-pass filter response, and X_i is the molar fraction of species i. A comparison of the theoretical rotational spectrum $RS(\lambda)$ with the measured rotational intensity can yield a rotational temperature for each probe volume along the laser. Figure 5 shows theoretical synthesized spectra for air, and the long pass filter response $LP(\lambda)$, versus wavelength.

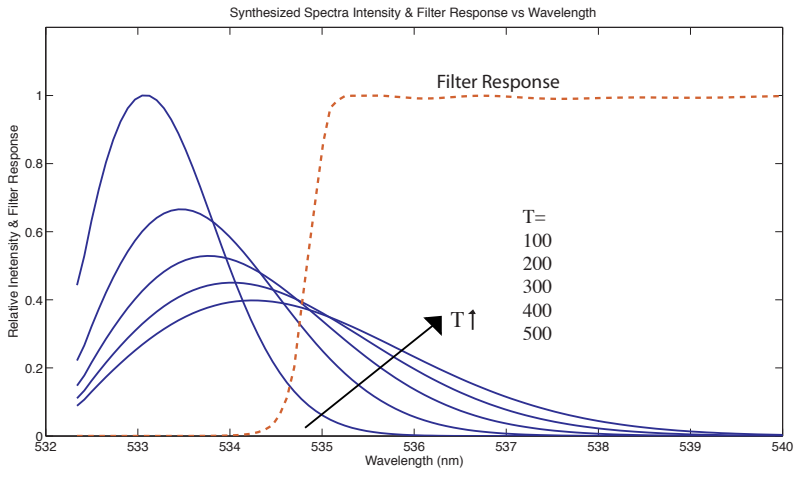

Figure 5. Plot of relative synthesized spectra intensity and the long pass filter response versus wavelength

Additionally, Fig. 6 shows the convolution of the filter response with the theoretical synthesized spectra for air. These filtered theoretical spectra are then compared to the collected rotational spectra in order to obtain temperature, and ultimately pressure measurements.

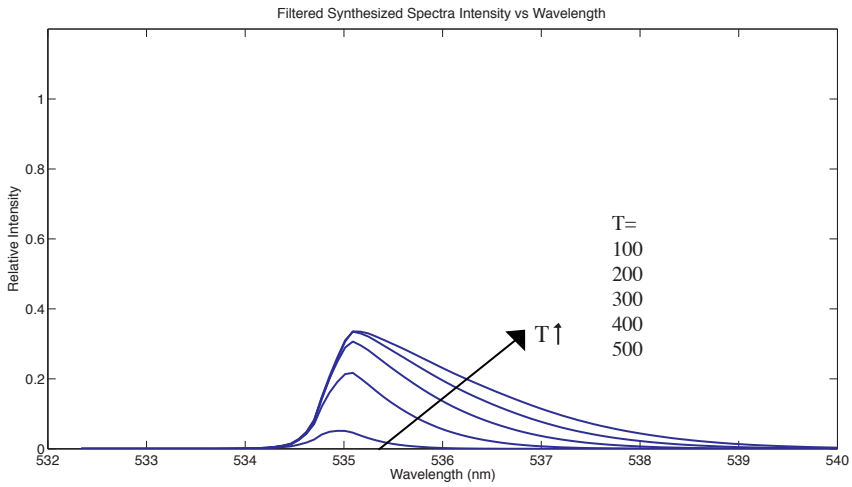

Figure 6. Plot of filtered synthesized spectra intensity versus wavelength

In the present air flow experiment the rotational constants of Both N_2 and O_2 molecules are lose in value and hence the rotational Boltzmann distributions of O_2 and N_2 are closely in along wavelength space. Therefore, their summation can be very closely approximated by a single exponential.

$$A_{O2}e^{-B_{O2}/T} + A_{N2}e^{-B_{N2}/T} \approx A_3 e^{-B_3/T} \tag{3.7}$$

When the long pass filter is convolved with the theoretical rotational spectra of air, the remaining spectra are much less than the original theoretical spectra, but still exhibit a temperature dependence as seen in Fig.6. Theoretical spectra for air were

synthesized for temperatures over a range of 100K to 500k, since this is primarily the temperature range being encountered in this experiment. The integrals of the filtered spectra were plotted versus the inverse of their corresponding temperature, and an exponential was found to be a close fit (Fig.7).As the number of samples of temperature increased between the range of 100K to 500K, the constant multiplying the inverse of temperature in the exponential asymptotically approached a value of -357.4 with units of degrees Kelvin to balance with the inverse of temperature. The resulting integration and exponential yields the following equation that was used for calculating temperature:

$$(\int I_{rot} d\lambda)/I_{N2} = Ce^{-357.4K/T} \tag{3.8}$$

Just as with the vibrational spectra calculations of density, the proportionality constant C accounts for a combination of different system parameters that can influence the amount of light received by the detector from the test section. This proportionality constant C can be calculated through calibration, or by the simultaneous measurement of known pressure and temperature conditions in some superpixel within the probe volume. The density adjusted rotational spectra is simply the rotational spectra divided through by the intensity N_2 vibrational spectra of the same probe volume. This eliminates amplitude effects of the rotational spectra due to density, and makes the integrated spectra non-dependent upon density. This is an important consideration that is made due to the synthesized spectra being non-dependent upon density. Once C was calculated using a superpixel with known conditions, temperature was then calculated for the rest of the laser probe by integrating the density adjusted rotational signal and solving Eqn.(3.8) for T.

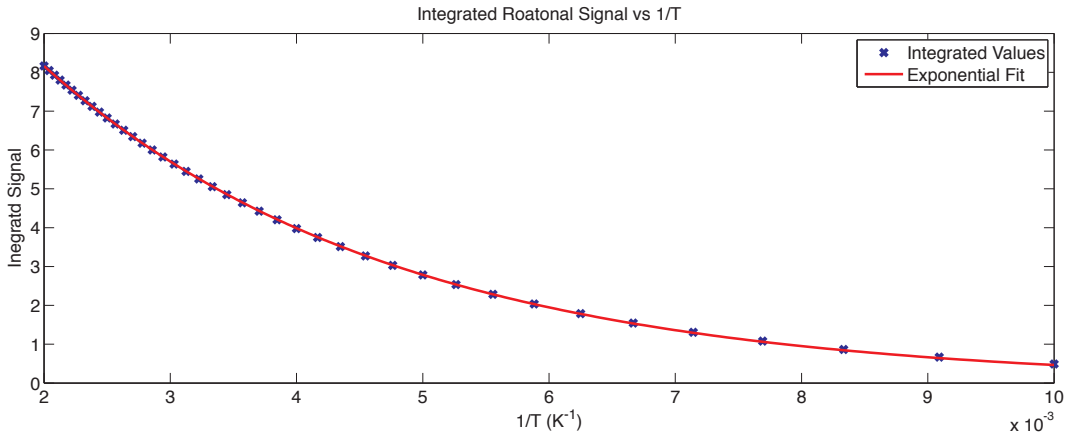

Figure 7. Integration of synthesized rotational spectra with filter applied vs inverse temperature

This independent measurement of temperature can then be converted to a local pressure measurement by using the ideal gas law along with the density measured by the vibrational Raman technique.

$$T = \frac{-357.4}{ln(\frac{\int I_{rot} d\lambda}{C I_{N2}})} \tag{3.9}$$

$$P = \rho R T \tag{3.10}$$

Two important advantages of the vibrational/rotational Raman combination are: (a) the technique yields a measurement for the rotational temperature, and the rotational degrees of freedom may safely be assumed at equilibrium in the conditions of the experiments, while the same may not be true for the vibrational degrees of freedom (Vincenti and Kruger, 1965); and (b) the relative strength of the rotational scattering cross-sections when compared to the vibrational ones, e.g. a factor of 7.5 in the case of N_2 (Eckbreth, 1988), yields a substantial improvement in the overall

SNR. The technique is superficially similar to past approaches that rely on Raman spectroscopy and spectral 'fitting', such as CARS (Cutler et al., 2003). The main advantage of the technique presented here is its inherent capability to produce spatially resolved measurements along a line, as well as provide a measurements of all major species, temperature, and pressure. The technique is a true multiscalar line measurement, as opposed to single-point temperature measurement techniques (CARS.)

3.3. Collected Spectra and Calculated Values

The experiment that was examined was the flow field of an exhaust issuing from an underexpanded jet nozzle with total pressure of 4 atmospheres (gauge), and an exit Mach number of approximately 2. In order to have data points for finding the coefficients A and C of Eqns.(3.1) & (3.8), respectively, the jet was moved as far right on the length axis as possible, while still completely being able to capture it with the spectrometer. It was then assumed that there were little effects of the jet on the left most column of super pixels, and thus further assumed that they represented the conditions of the lab (standard temperature and pressure). This left most column was the data set (spectra) (Fig.8) that was used to calculate the coefficients A and C. The hardware pixel binning of the camera was such that 16 pixels were binned across in the physical space axis, and 2 pixels were binned vertically in the wavelength axis. This resulted in less read noise injection into the collected data, and a resolution of 256 μm in physical space along the laser axis by .5 nm along the wavelength axis.

Figure 9 (a) shows an averaged spectral image captured by the detector with the spatial axis along the horizontal, and wavelength along the vertical. In order to better examine the decay of the rotational spectra in amplitude, as well as in wavelength width, Fig. 9 (b) was created by extracting the rotational profile and placing the

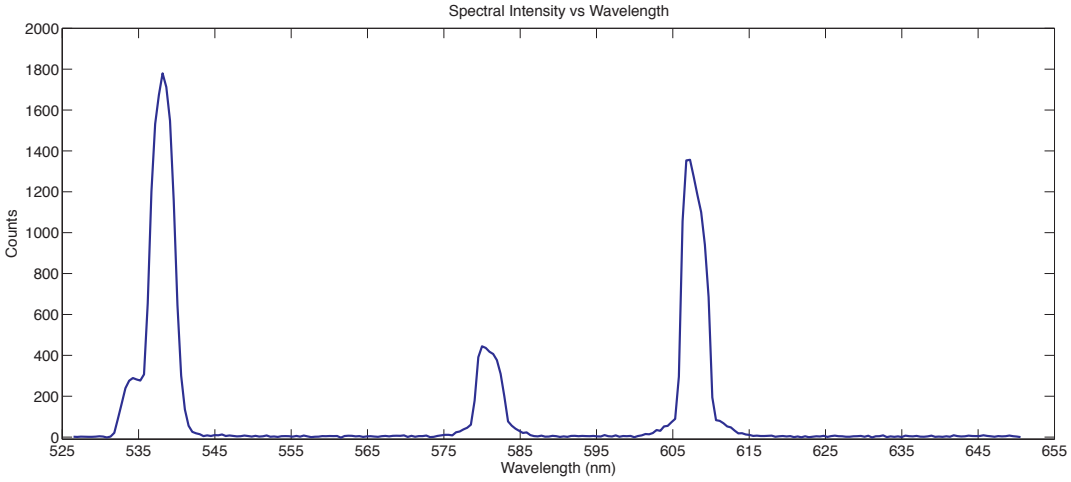

Figure 8. Plot of experimental calibration spectra intensity versus wavelength

extracted values into a 3-D plot. Symmetry in the spectra can be visually seen in both Figs. 9 (a) and (b), and this is expected due to the symmetry of the jet.

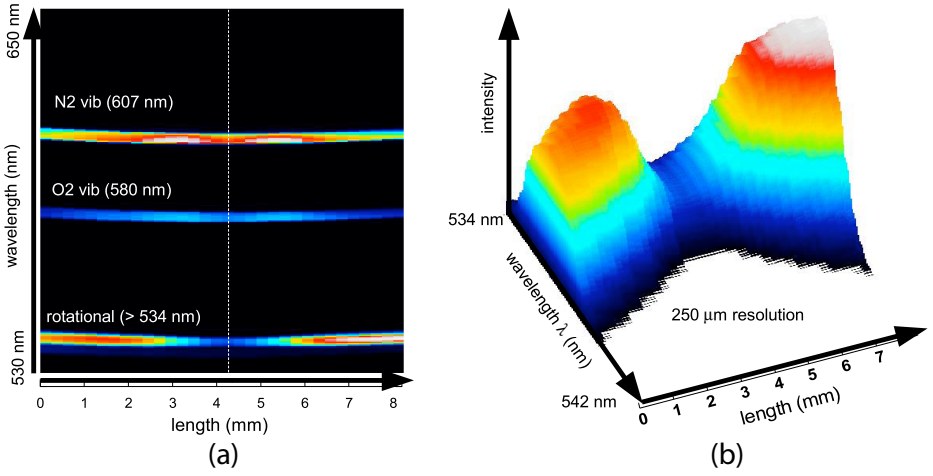

Figure 9. (a) Spectral image captured by the detector (b) Three dimensional close-up of the rotational spectra

The image was averaged over 93 individual images, however the initial data set contained originally 100 images. After filtering the images, 7 of them were determined to be unusable due to dielectric breakdown caused by dust in the lab. These sparks generated light that was able to propagate to detector, and resulted in false spectral images with extremely high counts. Each image, prior to averaging, was properly dark subtracted to eliminate background noise due to thermal effects of the detector. The experiment itself was performed in near complete darkness to reduce background noise as well.

3.4. Measurements and Calculation of Density, Temperature, and Pressure

Density measurements were calculated directly from the N_2 vibrational spectra (Fig.10) as described previously in the chapter using Eqn. (3.1). Likewise, temperature mea-

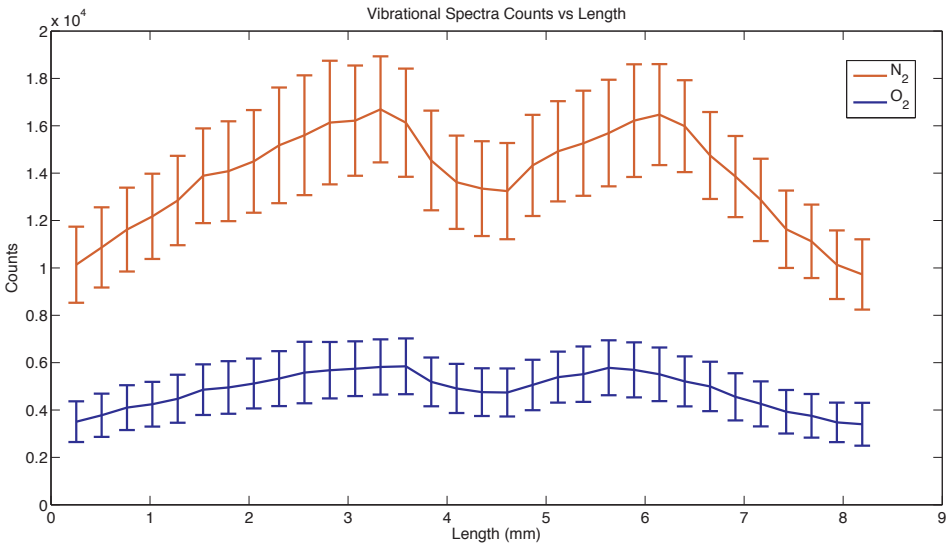

Figure 10. Integrated experimental vibrational profiles vs laser spatial axis (mm)

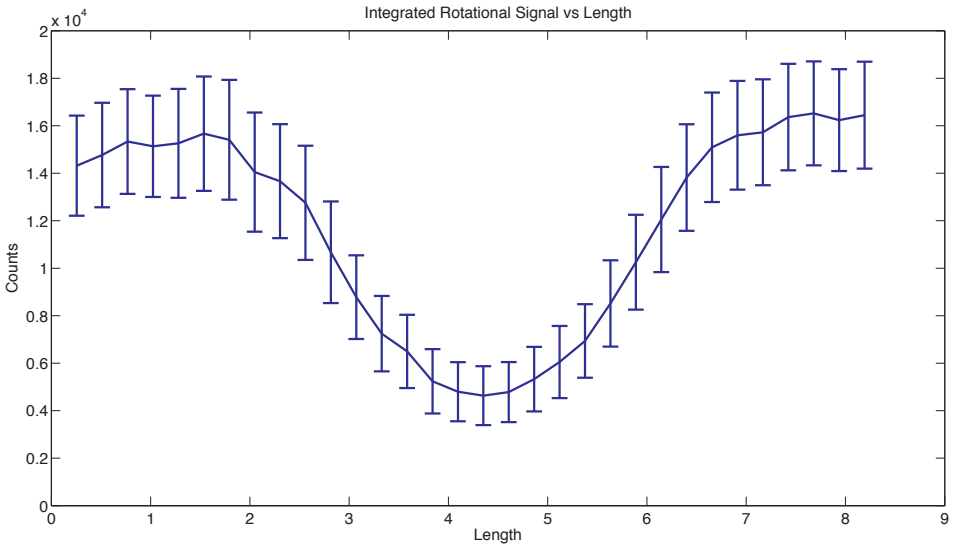

Figure 11. Integrated experimental rotational profiles vs laser spatial axis (mm)

surements were calculated from the integrated rotational spectra (Fig.11) using Eqn. (3.8). The left most probe volume was used to determine the coefficients A an C of these equations by assuming that the density for this probe volume was 1.2 kg/m^3, and also that the temperature was 300K. The error of each integrated signal was calculated by forming the standard deviation of the integrated signal of each probe volume the image over the range of the 93 collected images. Once the errors for the integrated N_2 vibrational spectra were calculated, the density and its associated errors were calculated as well since the density was directly proportional from the integrated N_2 signal, Fig. 12.

From here the once the rotational spectra was integrated, and its associated errors were calculated, the temperature distribution along the probe volumes could be determined as seen in Fig.14. The errors for temperature were calculated by taking the standard deviation of temperature for each probe volume over the range of the

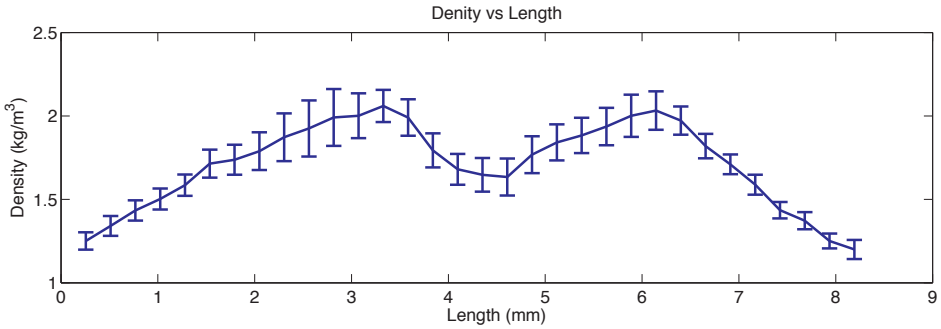

Figure 12. Calculated density (kg/m^3) vs laser spatial axis (mm)

93 collected images. An example of the variation in temperature from shot to shot can be seen in Fig.13.

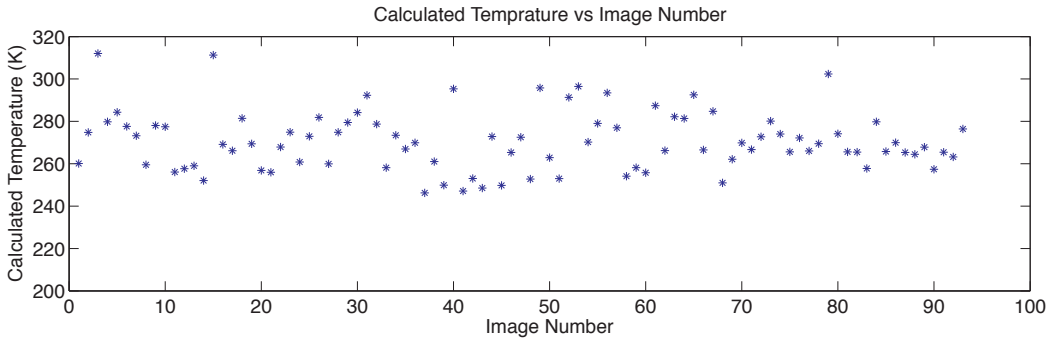

Figure 13. Sample calculated temperature vs image number at length = 1 mm

Finally, to calculate pressure, the ideal gas law was used with the density and temperature measurements along all of the probe volumes of the laser axis. Error analysis as well for pressure was done by performing single shot statistics over the image collection. These are plotted along the spatial axis of the laser in Fig.15.

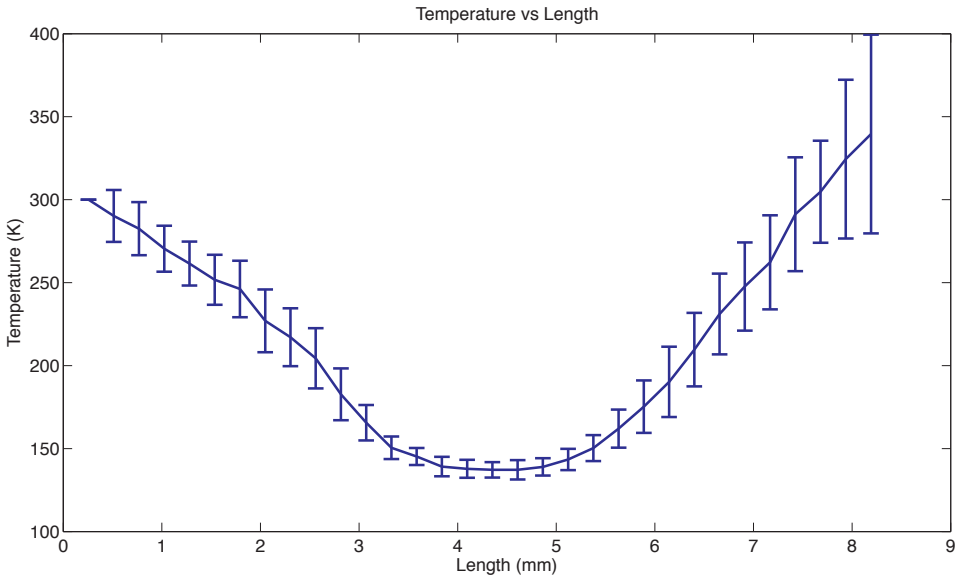

Figure 14. Calculated temperature (K) vs laser spatial axis (mm)

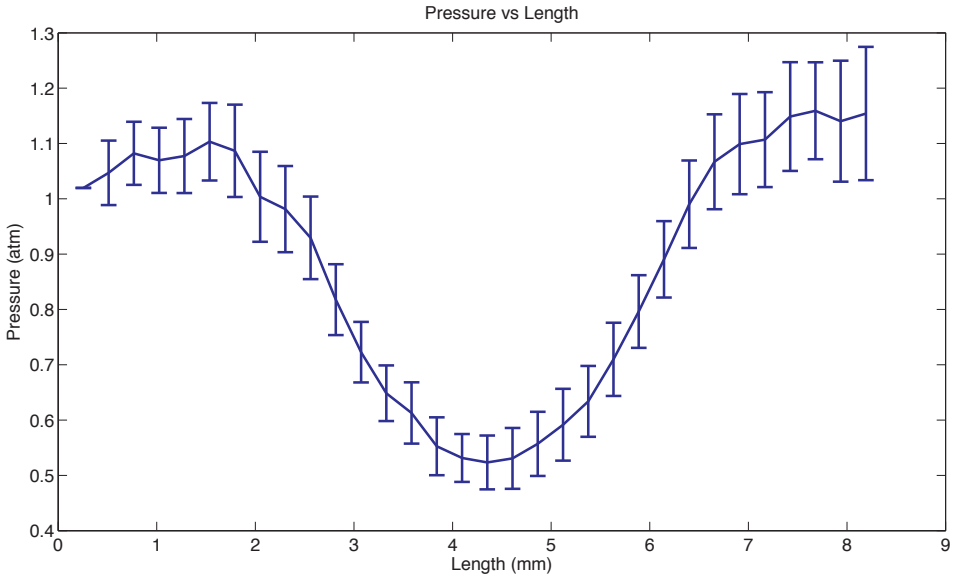

Figure 15. Calculated pressure (atm) vs laser spatial axis (mm)

3.5. Signal to Noise Ratio

The signal to noise ratio (SNR) of a collected spectra is defined to be the average of the spectral peak, divided by the standard deviation of the spectral peak (McCreery, 2000). The peak of each the N_2 vibrational, O_2 vibrational, and the rotational spectra were analyzed for each column of pixels (probe volume) for every one of the 93 individual images that were collected. The peaks of each spectra, for each probe volume were then averaged over the set of 93 images, and the standard deviation of these peaks were calculated in the same manner as well. The average SNR values for the N_2 and O_2 vibrational as well as the Rotational spectra over the range of all the probe volumes and 93 images were 13, 9, and 10 respectively.

3.6. Discussion

This behavior points to a measurement location before the reflected shock waves, i.e. in regions where the expansion fans lead to overexpansion at the centerline, and can be seen in Fig. 16. At the exit of an underexpanded jet a Prandtl-Meyer expansion fan radiates from the nozzle tip. A gas element flowing in the center region of the jet encounters the combined effect of expansions emanating from all over the exit periphery, and hence overexpansion ($p < P_{atm}$) ensues in the jet centerline as evidenced by the measurements in Fig.15 due to the interacting expansion waves. At the same time the free surface at the jet periphery acts as a boundary condition at higher pressure (P_{atm}) and compression waves are generated at the periphery and radiate inwards, until they coalesce into oblique shock waves that re-compress the flow to an underexpanded condition ($p > P_{atm}$). This is also evident in the data presented in Fig.15. The two oblique shock waves interact at the jet centerline and the refracted (or reflected) shock waves that result create an underexpanded supersonic jet flow that

repeats itself. The pressure and temperature measurements for the right most probe volumes, however, seem to be affected in a way that inflates the temperature, and therefore the pressure as well.

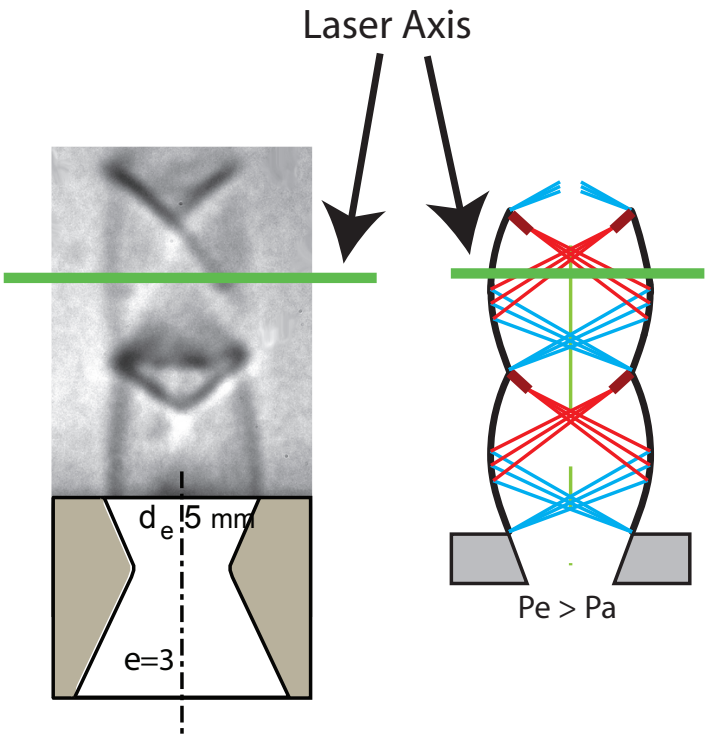

Figure 16. Schlieren image and diagram indicating region of examination

When examining Fig.9 (a), it can be seen that the right most columns of the image suffer from optical aberrations that tend to "squeeze" the spectra together, and this "squeezing" of the rotational signal seems to have increased its integrated value. This could possibly be to absorbing part of the Rayleigh signal that made it through the filter due to the experiment being very close to the nozzle. By having the

laser axis close to the nozzle, reflections of 532 nm from the nozzle make their way into the spectrometer and get interpreted as Rayleigh signal. However, the signal was substantially strong enough to still make it through the filter, and this can be seen in Fig.8 when examining the rotational profile at around 534 nm. The small lobe to the left of the rotational spectra is the reflected laser light due to the nozzle constructed from brass stock. When this extra lobe becomes squeezed with the rotational spectra, as it appears to be happening, this would then be interpreted as a high rotational value, and thus lead to higher temperature and pressure measurements as seen in Figs. 14 & 15 on the right.

A way to decrease the error bars on the measurement is to properly do image normalization as mentioned in the experimental setup. As the lab was for this experiment, it was nor ready for shot normalization, and therefore the laser intensity variation from shot to shot contributed to the uncertainty of the process. Once shot normalization begins to occur, the error with decrease, and the SNR will also increase at the same time. Overall, because these shots were not normalized, and this is the first set of data collected by the system, the final density, temperature, and pressure results presented should be consider purely as qualitative rather than quantitative due to the nature of their large errors.

3.7. Future Work

Future work immediately will focus on improving the quality of the system. This can be done by trying to minimize optical aberrations, normalize each collected spectral image with its associated shot intensity, perform calibrations of the system on a continuous basis, and eventually get the system to be able to take single-shot measurements rather than averaged measurements. Temperature measurements in the

future, also, will be done based on actually fitting a theoretical spectra to the actual obtained rotational spectra rather than fitting an exponential to the integral of the rotational spectra itself. A more long term for future work will be aimed at studying reacting flows from underexpanded jet nozzles, and studying the turbulence-chemistry interactions associated with flame suppression. One of the most important goals of the line imaging system constructed is the capability to take measurements of conserved scalars ξ and their dissipation rates χ. Being able to obtain this data along with the thermochemistry measurements of the flow will allow for the study of flow-chemistry interaction, as well as how it is affected by different pressures.

REFERENCES

Bilger, R., Starner, S., and Kee, R. (1990) On the reduced mechanisms for methane-air combustion in non-premixed flames. *Combustion and Flame*, **80**, 135.

Chen, Y. and Mansour, M. (1997) Measurements of scalar dissipation in turbulent hydrogen diffusion flames and some implications on combustion modeling. *Combustion Science and Technology*, **126**, 291.

Cheng, T., Yuan, T., Lu, C.C., and Chao, Y.C. (2002) The application of spontaneous vibrational Raman scattering for temperature measurements in high pressure laminar flames. *Combustion Science and Technology*, **174**, 111.

Cutler, A., Danehy, P., and RR, P.S. (2003) Coherent anti-stokes Raman spectroscopic thermometry in a supersonic combustor. *AIAA Journal*, **41**, 2451.

Eckbreth, A. (1988) *Laser Diagnostics*. Abacus Press, Cambridge, MA.

Fernández, J., Punge, A., Tejeda, G., and Montero, S. (2006) Quantitative diagnostics of a methane/air mini-flame by Raman spectroscopy. *Journal of Raman Spectroscopy*, **37**, 175.

Foglesong, R., Green, S., Lucht, R., and Dutton, J. (1998) Dual-pump coherent anti-Stokes Raman scattering for simultaneous pressure/temperature measurement. *AIAA Journal*, **36**, 234.

Forkey, J., Lempert, W., and Miles, R. (1998) Accuracy limits for planar measurements of flow field velocity, temperature and pressure using filtered Rayleigh scattering. *Experiments in Fluids*, **24**, 151.

Fowles, G. (1989) *Introduction to Modern Optics*. Dover Publications, New York, NY.

Hassel, E. and Linow, S. (2000) Laser diagnostics for studies of turbulent combustion.

Measurement Science and Technology, **11**, 37.

John, J. and Keith, T. (2006) *Gas Dynamics*. 3rd edition, Pearson Education Inc., Upper Saddle River, NJ.

Karpetis, A.N. and Barlow, R.S. (2003) Measurements of scalar dissipation in a turbulent piloted methane/air jet flame. *Proceedings of the Combustion Institute*, **29**, 1929.

Kojima, J. and Nguyen, Q.V. (2004) Measurement and simulation of spontaneous Raman scattering in high-pressure fuel-rich H_2-air flames. *Measurement Science and Technology*, **15**, 565.

Laurendeau, N. (1988) Temperature measurements by light-scattering methods. *Progress in Energy and Combustion Science*, **14**, 147.

Linán, A. and Williams, F. (1993) *Fundamental Aspects of Combustion*. Oxford University Press, Oxford, UK.

Mackay, C., Tubbs, R., Bell, R., Burt, D., and Moody, I. (2001) Sub-electron read noise at MHz pixel rates. *Proceedings of SPIE, Int.Soc.Opt.Eng.*, **4306**, 289.

Masri, A., Dibble, R., and Barlow, R. (1996) The structure of turbulent nonpremixed flames revealed by Raman-Rayleigh-LIF measurements. *Progress in Energy and Combustion Science*, **22**, 307.

McCreery, R. (2000) *Raman Spectroscopy for Chemical Analysis*. John Wiley and Sons, Inc., New York, NY.

Miles, P. and Barlow, R. (2000) A fast mechanical shutter for spectroscopic applications. *Measurement Science and Technology*, **11**, 392.

Miles, R., Lempert, W., and Forkey, J. (2001) Laser Rayleigh scattering. *Measurement Science and Technology*, **12**, R33.

Nandula, S., Brown, T., Pitz, R., and Debarber, P. (1994) Single-pulse, simultane-

ous multipoint multispecies Raman measurements in turbulent nonpremixed jet flames. *Optics Letters*, **19**, 414.

Nguen, Q., Dibble, R., Carter, C., Fiechtner, G., and Barlow, R. (1996) Raman-LIF measurements of temperature, major species, OH, and NO in a methane-air Bunsen flame. *Combustion and Flame*, **105**, 499.

Schrader, B. (1995) *Infrared and Raman Spectroscopy*. VCH Publishers Inc., New York, NY.

Tejeda, G., Mate, B., Fernandez-Sanchez, J., and Montero, S. (1996) Temperature and density mapping of supersonic jet expansions using linear Raman spectroscopy. *Physical Review Letters*, **76**, 34.

Vincenti, W. and Kruger, C. (1965) *Introduction to Physical Gas Dynamics*. John Wiley & Sons, New York, NY.

Zhou, S., Lin, Z., and Jiang, X. (2007) Beam smoothing by lens array with spectral dispersion. *Optics Letters*, **272**, 186.

VITA

Name:	Alexander Christian Bayeh
Address:	Department of Aerospace Engineering
	701 H.R. Bright Building, Ross St.- TAMU 3141
	College Station, TX 77843-3141
Email Address:	Abayeh@tamu.edu
Education:	B.S., Aerospace Engineering, Texas A&M University, 2008
	M.S., Aerospace Engineering, Texas A&M University, 2009

.